Check for updates

Coordinated water modulation for proton conductivity *via* post-synthetic transmetalation in yttrium-based coordination polymers

Byoung Gwan Lee, [iD] [a] Dongwook Kim,[b] Jin Young Bae, [iD] [a] Ji Woo Jeong [iD] [a] and Dae-Woon Lim [iD] *[a]

Understanding the correlation between structural variations and proton transport in coordination polymers (CPs) is essential for developing efficient solid-state proton conductors (SSPCs). In this study, we demonstrate that post-synthetic transmetalation *via* alkali metal exchange enhances proton conductivity in a pseudo-three-dimensional yttrium-based CP, $\{[Y(H_2O)_4(HDSNDC)] \cdot H_2O\}_n$ (H_4DSNDC = 4,8-disulfonaphthalene-2,6-dicarboxylic acid). Immersion in 1 M KCl solution induces transmetalation, yielding a potassium-substituted analogue, $\{K_3(H_2O)_2(HDSNDC)\}_n$. Structural analysis reveals that transmetalation induces structural reorganization, in which terminal H_2O ligands are converted into μ-bridging ones. These bridging H_2O ligands exhibit increased acidity due to cooperative polarization by adjacent K^+ ions, facilitating proton dissociation and significantly enhancing conductivity from 7.23×10^{-5} S cm^{-1} for Y-DSNDC to 2.50×10^{-3} S cm^{-1} for K-DSNDC at 363 K under 95% RH. This work highlights transmetalation-induced coordination tuning as an effective strategy to enhance proton transport in CPs.

The depletion of fossil fuels and accelerating climate change driven by carbon emissions and greenhouse effects highlight the urgent demand for carbon neutrality and eco-friendly energy platforms. In particular, proton exchange membrane fuel cell (PEMFC) systems, which convert chemical energy to electrical energy, have attracted significant attention as sustainable energy platforms due to their high energy efficiency, zero carbon emission, and utilization of sustainable energy sources.[1,2] Specifically, one of the key components in PEMFCs is proton exchange membranes (PEMs), a solid-state electrolyte, whose conductivity and durability significantly influence device performance.[3] To date, perfluorosulfonic acid-based organic polymer membranes, such as Nafion, are well-known conventional

solid-state proton conductors.[4,5] However, their high cost and performance degradation under dry or high-temperature conditions, due to limited stability, require alternative solid-state electrolytes.[6–8]

Recently, coordination polymers(CPs), constructed by coordination bonds between metal ions and organic linkers, have garnered increasing attention as solid-state proton conductors owing to their structural designability, tunability, thermal stability, and superior proton transport properties under mild temperature conditions.[9–16] To enhance their proton conductivity, various strategies have been explored, including the introduction of predesigned functionality in the frameworks *via de novo* synthesis[17,18] (*e.g.*, employing the ligands including extra acidic functional groups) and post-synthetic metal and ligand modifications, such as controlling the coordination environment of metal centres,[19,20] incorporating hydrophilic acid functional groups in the ligands (*e.g.*, $-SO_3H$, $-COOH$, $-PO_3H_2$),[21,22] and introducing guest molecules such as H_2O, NH_3, imidazole, and inorganic acids.[23–27] These approaches have not only facilitated hydrogen bonding networks but also increased the mobile proton concentration.[28,29] While these strategies have shown promise, they do not inherently guarantee efficient proton conduction. The effectiveness often depends on the spatial arrangement and chemical composition of the resulting conduction pathways. The decisive factor for high conductivity lies not merely in the presence of conducting media (*e.g.*, H_2O, NH_3, or acids) and functional groups, but in how these components cooperate to create geometrically favourable and dynamically interactive environments for proton diffusion. Therefore, structural designs that promote the formation of conjugated acid–base systems, such as $H_3O^+ + H_2O \rightleftharpoons H_2O + H_3O^+$ or $OH^- + H_2O \rightleftharpoons H_2O + OH^-$ between guest molecules and nearby acidic or basic sites, can be more critical for facilitating efficient proton transport.[30–33] Among emerging strategies to engineer such environments, post-synthetic metal ion exchange (transmetalation) has attracted considerable attention for its ability to modulate local
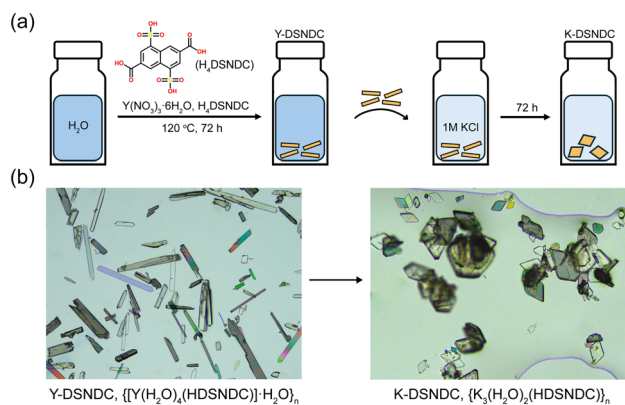
[a] Department of Chemistry, Yonsei University, 1 Yonseidae-gil, Wonju, Gangwon-do 26493, Republic of Korea. E-mail: limdaewoon@yonsei.ac.kr
[b] Center for Catalytic Hydrocarbon FunctionalizationInstitute of Basic Science, Daejeon 34141, Republic of Korea

coordination environments while preserving crystallinity *via* solution-mediated transmetalation.[34–36] In this approach, the coordination mode of H_2O molecules, whether terminal or bridging, can often be modulated, leading to variations in their pK_a. Notably, the replacement of high valence metal centres with alkali metal cations, which possess lower valency and large ionic radii, enables high metal ion densities, thereby favouring the formation of μ-bridging water ligands between adjacent centres.[37–39] These bridging waters exhibit enhanced acidity due to cooperative polarization, which strengthens hydrogen-bond networks and increases their proton-donating ability, thereby increasing the concentration of mobile protons.[40–42] Although structural modulation *via* transmetalation is a promising approach to promote efficient proton conduction, to the best of our knowledge, there are scarce reports, and the detailed mechanistic understanding of how exchanged alkali ions govern proton transport remains incomplete. Herein, we demonstrate an enhancement in proton conductivity of Y-DSNDC $\{[Y(H_2O)_4(HDSNDC)]\cdot H_2O\}_n$ (H$_4$DSNDC = 4,8-disulfonaphthalene-2,6-dicarboxylic acid) *via* transmetalation with K^+ under ambient conditions, resulting in $\{K_3(H_2O)_2(HDSNDC)\}_n$ (Scheme 1). During the process, four terminally coordinated H_2O molecules in $\{[Y(H_2O)_4(HDSNDC)]\cdot H_2O\}_n$ were changed to two bridging H_2O (μ-H_2O) ligands protruding into the pore direction and exhibiting an improved proton conductivity from 7.23×10^{-5} to 2.50×10^{-3} S cm^{-1} at 363 K.

Two structurally defined coordination polymers, Y-DSNDC $\{[Y(H_2O)_4(HDSNDC)]\cdot H_2O\}_n$ and its metal-exchanged analogue K-DSNDC $\{K_3(H_2O)_2(HDSNDC)\}_n$, were synthesized using H$_4$DSNDC, a sulfonic acid-functionalized naphthalene dicarboxylic acid ligand. The dual –SO$_3$H/–COOH functionality of the ligand can enhance its hydrophilicity, thereby promoting dense hydrogen-bonding networks essential for proton conduction. Y-DSNDC was obtained as single crystals *via* a hydrothermal reaction using Y(NO$_3$)$_3$·6H$_2$O and H$_4$DSNDC at 120 °C. Single-crystal X-ray structural analysis reveals that Y-DSNDC has a monoclinic crystal system with the $P2_1/m$ space group

(Table S1). The coordination of yttrium ions and H$_4$DSNDC extends the structure along the *bc* plane, forming a 2D framework, incorporating one lattice H_2O molecule. The two carboxyl groups of HDSNDC each coordinate to yttrium ions in the *ac* plane in a monodentate fashion, with the coordinating oxygen atoms originating from the carbonyl (C=O) moieties. One carboxyl group is deprotonated (–COO$^-$), while the other remains protonated (–COOH) and forms a hydrogen bond with the adjacent carboxylic acid and carboxylate groups (O···O = 2.552 Å) (Fig. S2). One of the two sulfonate functional groups remains uncoordinated, while the other bridges yttrium ions along the *b*-axis (Fig. 1c). Specifically, Y1 exhibits eight-coordinate geometry, coordinated by four terminal H_2O molecules (O24, O25, O26, O26*), two oxygen atoms from two sulfonate groups (O16, O16*), and two oxygen atoms from the carboxylate group (O19) and carboxylic acid group (O23) of the HDSNDC ligands (Fig. 1a). The Y1–O bond lengths range from 2.237 to 2.439 Å. According to continuous shape measurement (CShM) calculations of metal coordination geometry using the SHAPE software (Table S2),[43] the coordination geometry of Y1 approximates a triangular dodecahedron. When viewed along the *c*-axis, the yttrium centres are arranged in a zigzag pattern along the *b*-axis (Fig. 1c). The *bc* planes are interconnected through hydrogen bonding between the terminally coordinated H_2O molecules and the uncoordinated sulfonate functional group along the *a*-axis. Overall, a two-dimensional coordination network of metal ions and ligands forms a pseudo-three-dimensional structure through interlayer hydrogen bonding (Fig. S3). Hydrogen bonding between the ligand and coordinated H_2O molecules along the *b*-axis exhibits distances of 2.675 and 2.824 Å (O$_{H_2O}$···O$_{SO_3^-}$) (Fig. S6b). The ligand molecules are planar and oriented parallel to the *ac*-plane, generating rectangular pores extending along the *c*-axis (6.8 × 3.4 Å, Fig. 1c). As shown in Scheme 1 and Fig. S4, immersing the rod-shaped

Scheme 1 (a) Schematic illustration of the transmetalation process. (b) Crystal images of Y-DSNDC (left) and K-DSNDC (right).
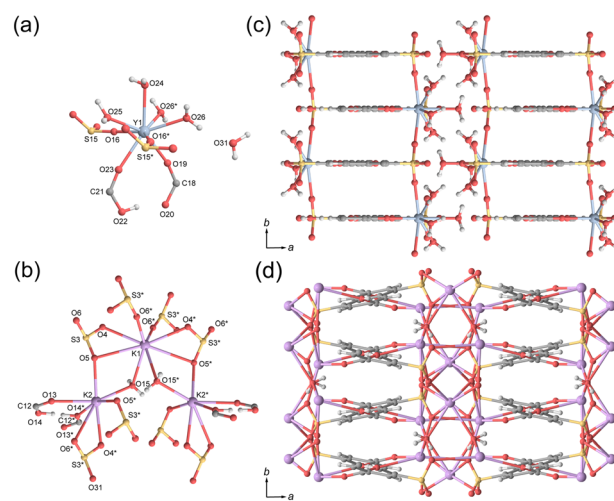

Fig. 1 The coordination environment of the (a) Y^{3+} ion and (b) K^+ ions. The cell packing along the *c*-axis of (c) Y-DSNDC and (d) K-DSNDC.

Y-DSNDC crystals in a 1 M aqueous KCl solution for 72 hours induces time-dependent transmetalation, gradually transforming them into plate-shaped K-DSNDC. K-DSNDC crystals could not be directly synthesized under the same conditions. Single-crystal X-ray diffraction analysis reveals that K-DSNDC retains the monoclinic crystal system but adopts a different space group, $C2/c$ (Table S1). For charge balance, one trivalent Y^{3+} was substituted by three monovalent K^+ ions, resulting in a reorganization of the coordination environment. A metal cluster is formed with two distinct K^+ coordination geometries, and terminally coordinated H_2O molecules in Y-DSNDC are converted to μ-bridging H_2O ligands. Furthermore, all sulfonate functional groups in the ligands coordinate to metal centres, resulting in 3D networks. Within the metal cluster, K1 adopts an eight-coordinate biaugmented trigonal prismatic geometry. It is coordinated by two μ-H_2O molecules (O15, O15*) that bridge K1 with K2 and K2*, four oxygen atoms from two sulfonate ligands acting in a bidentate mode (O4, O5, O4*, O5*), and two oxygen atoms (O6*) from two monodentate sulfonate groups, as shown in Fig. 1b. In contrast, K2 adopts a seven-coordinate capped octahedral geometry, bonded to one μ-H_2O (O15), one monodentate sulfonate oxygen (O5*), two oxygens from bidentate sulfonate (O4*, O6*), one μ-bridging sulfonate oxygen (O5), and two monodentate oxygens from carboxylic acids (O13, O14*). The orientation of the ligands remains similar to that of Y-DSNDC, with adjacent carboxylate groups of ligands in K-DSNDC connected along the c-axis through O–H···O hydrogen bonding (O···O = 2.470 Å) (Fig. S6). Although the ligands lie parallel to the ac-planes, they exhibit a torsion angle of 28.6° between the naphthalene rings and carboxylic acid groups due to coordination of all oxygen atoms in $–SO_3^-$ functional groups, resulting in a tilted stacking configuration. This conformational change enlarges the one-dimensional rectangular pores along the c-axis, yielding channels approximately 7.3 Å wide and 3.6 Å high (Fig. 1d).

The powder X-ray diffraction (PXRD) patterns of the as-synthesized Y-DSNDC and after immersion of Y-DSNDC crystals in 1 M aqueous KCl solution for 72 hours are equivalent to the simulated patterns obtained from single-crystal X-ray data, confirming the successful formation of a phase-pure crystalline material. This is consistent with recrystallization into a new phase via transmetalation, without any detectable remnants of the original Y-DSNDC phase (Fig. 2). Both coordination polymers exhibit high chemical stability in water and common organic solvents (Fig. S9). In the FT-IR spectrum of H_4DSNDC, the C=O stretching band appears at 1695 cm^{-1}. Upon coordination to Y^{3+} and K^+, this band shifts to 1683 and 1682 cm^{-1}, respectively, confirming metal-carboxylate bond formation. In addition, the free ligand shows characteristic sulfonic acid vibrations at 1192, 1112, and 1046 cm^{-1}, corresponding to S=O and S–O stretching modes. In Y-DSNDC, these bands
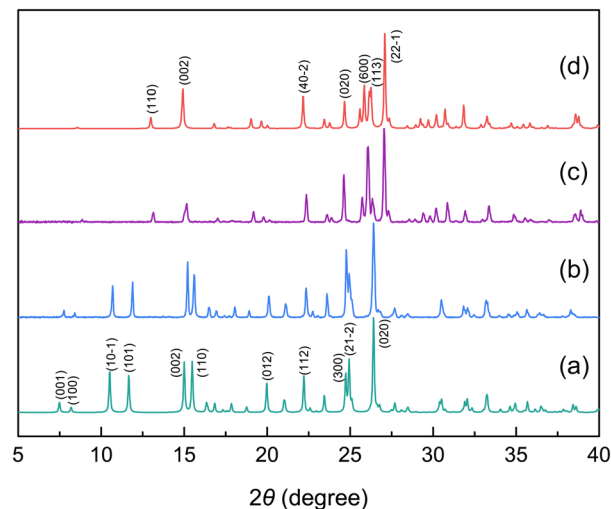

Fig. 2 Powder X-ray diffraction (PXRD) patterns. (a) Simulated pattern of Y-DSNDC from single-crystal X-ray data. (b) As-synthesized Y-DSNDC. (c) As-synthesized K-DSNDC. (d) Simulated pattern of K-DSNDC from single-crystal X-ray data.

are split and shifted into distinct pairs at 1195/1164, 1115/1089, and 1054/1025 cm^{-1}. This splitting arises from the coexistence of coordinated and non-coordinated sulfonate groups within the structure (Fig. S1a), resulting in asymmetric vibrational environments in line with previous reports.[44] In K-DSNDC, vibration characteristics of sulfonate groups are observed at 1191, 1116, and 1044 cm^{-1}, confirming the presence of sulfonate groups in the framework (Fig. S11).

The structural features of Y-DSNDC and K-DSNDC are further supported by X-ray photoelectron spectroscopy (XPS) analysis (Fig. S12 and S13). In Y-DSNDC, the S 2p region exhibits two distinct doublets, indicative of asymmetric coordination of the sulfonate groups, in agreement with the IR spectral splitting and the single-crystal X-ray structure. In contrast, K-DSNDC exhibits a single S 2p doublet, reflecting a uniform coordination environment. Both compounds exhibit excellent thermal stability in thermogravimetric analysis (TGA), as evidenced by structural decomposition occurring only above 450 °C. The initial weight loss below 200 °C arises from the release of lattice and coordinated water molecules, which is fully reversible. Y-DSNDC shows a three-step weight loss of approximately 15% below 200 °C, consistent with five water molecules in the structure (calculated value: 16.3%). The first step, approximately 6% below 90 °C, corresponds to the release of two molecules, followed by another 6% up to 150 °C, and a final 3% by 200 °C. In contrast, K-DSNDC exhibits a single weight loss of 6.89% between 110 and 150 °C, consistent with the loss of two bridging water molecules (calculated: 6.8%) (Fig. S14). To confirm the porosity, N_2 gas sorption measurements were carried out at 77 K. Neither sample exhibits significant N_2 uptake in the low-pressure region ($P/P_0 < 0.2$), consistent with the single-crystal X-ray structures indicating pore apertures smaller than the kinetic
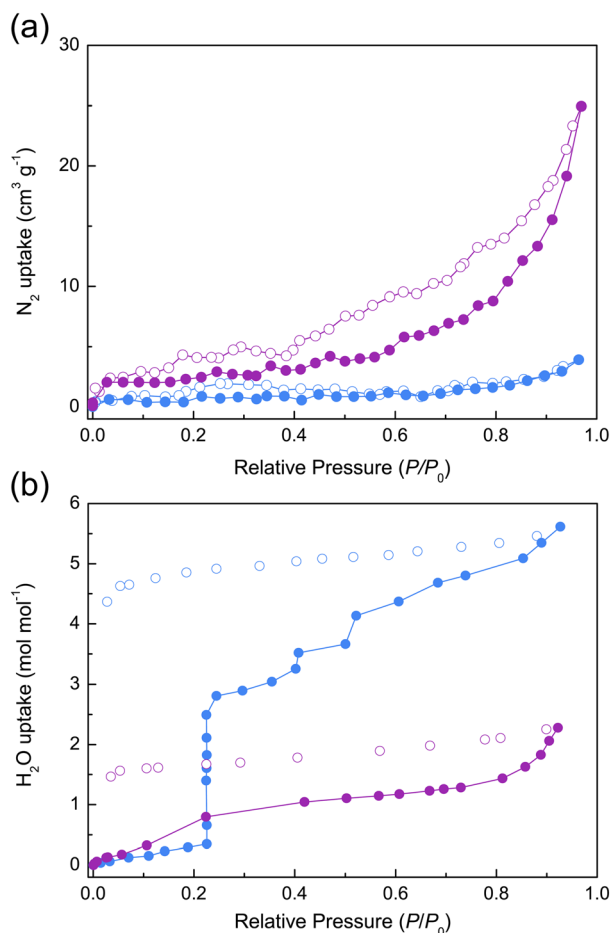
(a)

(b)

Fig. 3 (a) N_2 sorption isotherms at 77 K and (b) H_2O vapor sorption isotherms at 298 K for Y-DSNDC (blue) and K-DSNDC (purple). Filled circles represent adsorption and open circles represent desorption.

diameter of N_2 (3.64 Å). However, K-DSNDC shows a pronounced increase in uptake near saturation ($P/P_0 \approx 1.0$), which can be attributed to multilayer adsorption on the external surface or condensation within interparticle voids (Fig. 3a).[45] To further investigate the hydration behaviour, H_2O vapor sorption measurements were carried out after thermal activation at 373 K for 24 h under vacuum. During this process, the removal of lattice and coordinated water induced structural changes, as confirmed by PXRD (Fig. S15). H_2O vapor sorption isotherms recorded at 298 K revealed stepwise uptake in both materials with increasing relative humidity (RH). Y-DSNDC adsorbed up to 5.6 H_2O molecules per formula unit until $P/P_0 = 0.95$, of which approximately 5 H_2O molecules remained after desorption, indicating strong retention within the framework. Similarly, K-DSNDC uptakes 2.3 H_2O molecules per formula unit and retains approximately 2 H_2O molecules upon desorption. In both cases, PXRD patterns collected after H_2O vapor sorption revealed a full structural recovery to the original structure, suggesting reversible framework rehydration driven by water incorporation (Fig. 3b and S15). To further investigate the uptake behaviour and host–guest interactions of water

molecules after structural recovery, second-cycle H_2O vapor sorption measurements were conducted. Second-cycle H_2O vapor sorption measurements revealed that K-DSNDC exhibited slightly higher uptake of guest water molecules than Y-DSNDC in the range of P/P_0 = 0.1–0.8, which is attributed to its expanded pore dimensions as shown in structural analysis. In addition, the steep uptake observed for K-DSNDC at $P/P_0 \approx 0.9$ can be ascribed to multilayer adsorption in the pore. A hysteresis loop between the adsorption and desorption branches was observed, consistent with the thermodynamic irreversibility of capillary condensation, which means the presence of strong interaction sites with guest water molecules in the pores.[46] This behaviour may also be influenced by the slow desorption of water molecules due to strong hydrogen bonding interactions within the framework (Fig. S16). Based on the structural analysis, this phenomenon can be attributed to the μ-bridging H_2O molecules protruding into the pore direction. The structural modifications induced by metal exchange, including expanded pore dimensions and changes in metal-aqua coordination environments, provided a compelling rationale to investigate their impact on proton conductivity. For proton conductivity measurements, pelletized samples of Y-DSNDC and K-DSNDC were analyzed using electrochemical impedance spectroscopy (EIS) under variable relative humidity (RH) and temperature conditions. As shown in Fig. 4a, proton conductivity was measured at 298 K while increasing the relative humidity from 30% to 95%. At 30% RH, Y-DSNDC exhibited a conductivity of 9.19×10^{-11} S cm^{-1}, while K-DSNDC showed a markedly higher value of 2.44×10^{-8} S cm^{-1}. Under low-humidity conditions, the higher conductivity of K-DSNDC compared to Y-DSNDC can be attributed to the lower pK_a of μ-bridging H_2O molecules, despite Y-DSNDC containing more terminally coordinated H_2O. As humidity increased, the proton conductivities of both materials showed strong moisture dependence, reaching 1.56×10^{-4} S cm^{-1} for Y-DSNDC and 2.89×10^{-4} S cm^{-1} for K-DSNDC, respectively, at 95% RH. The temperature-dependent proton conductivities at 95% RH are presented in Fig. 4b. Y-DSNDC exhibits a gradual increase in conductivity with rising temperature, reaching a maximum of 2.55×10^{-4} S cm^{-1} at 343 K. Above this point, the conductivity progressively declined, reaching 7.23×10^{-5} S cm^{-1} at 363 K. In contrast, K-DSNDC shows a continuous increase, attaining 2.5×10^{-3} S cm^{-1} at 363 K (Fig. 4c). Activation energies (E_a), derived from Arrhenius plots, were 0.13 eV for Y-DSNDC and 0.30 eV for K-DSNDC, consistent with the Grotthuss-type proton diffusion, where protons migrate via hydrogen-bond-assisted hopping (Fig. 4b). Notably, the maximum proton conductivity of K-DSNDC (2.5×10^{-3} S cm^{-1} at 363 K and 95% RH) surpasses the highest values reported for K-based CPs or MOFs, including the 3D frameworks $[K_2(OOCCH(OH)PO_3H)(H_2O)_2]$ (K-HPAA) (1.3×10^{-3} S cm^{-1} at 297 K under 98% RH)[47] and $\{[K_8(PTC)_2(H_2O)_{1.5}]\cdot4H_2O\}_n$ (1.0×10^{-3} S cm^{-1} at 298 K under 98% RH),[48] highlighting its outstanding proton transport performance among K-based materials. In Y-DSNDC, the
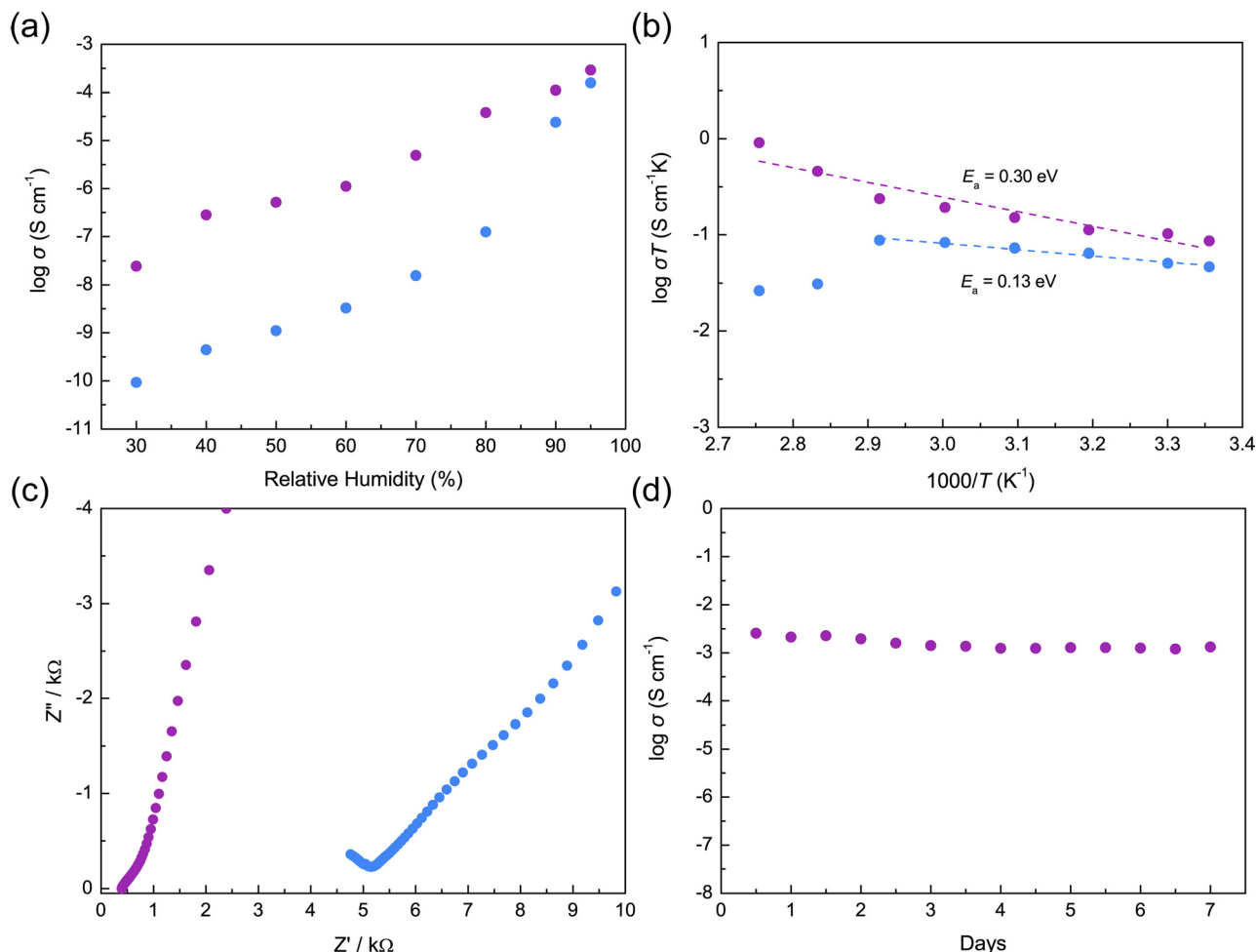
Fig. 4 (a) Humidity-dependent conductivity of Y-DSNDC (blue) and K-DSNDC (purple) measured at 298 K. (b) Arrhenius plots for Y-DSNDC (blue) and K-DSNDC (purple) in the temperature range of 298–363 K under 95% RH. (c) Nyquist plots of the highest conductivity for Y-DSNDC (blue) and K-DSNDC (purple) measured at 343 K and 363 K under 95% RH, respectively. (d) Long-term stability of the proton conductivity for K-DSNDC at 363 K under 95% RH.

decrease in conductivity from 343 K to 363 K coincides with the release of two coordinated water molecules from the structure, as confirmed by TGA (Fig. S14). A comparison of the hydrogen-bonding environments around the Y^{3+} centre indicates that the two coordinated water molecules (O26, O26*) each form only two hydrogen bonds, the fewest among all structural water molecules, and are thus weakly bound and preferentially lost upon heating (Fig. S17). Their loss disrupts the hydrogen-bonding network, as shown in Fig. S18, leading to a decline in the proton transport pathway. Although PXRD analysis after EIS measurements at 363 K (Fig. S21) confirms that the overall crystalline framework remains intact, the removal of these water molecules significantly weakens the hydrogen-bonding network and diminishes proton transport efficiency. In contrast, K-DSNDC exhibited a continuous increase in proton conductivity with rising temperature, which reflects the thermal retention of tightly bound water molecules that preserve the hydrogen-bonding network. The superior proton conductivity of K-DSNDC across the entire humidity and temperature ranges,

relative to Y-DSNDC, can be ascribed to multiple structural advantages. First, the expanded pore apertures in K-DSNDC allow for greater uptake of guest water molecules, which enhances the formation of extended hydrogen-bonding networks. Second, μ-bridging water molecules are likely to exhibit higher acidity, facilitating proton dissociation and increasing the concentration of mobile protons. Finally, the spatial proximity between acidic bridging water molecules and guest water enables efficient hydrogen-bonded interactions that facilitate proton hopping (Fig. S22). Notably, no degradation in performance was observed over several days, suggesting that the proton conductivity of K-DSNDC remains stable in the long term (Fig. 4d).

Conclusions

In summary, two unprecedented coordination polymers, Y-DSNDC and its transmetalation analogue K-DSNDC, were synthesized using the sulfonic acid-functionalized organic linker H_4DSNDC (4,8-disulfonaphthalene-2,6-dicarboxylic acid). The

replacement of Y^{3+} with K^+ triggered a substantial reorganization of the metal coordination environment, resulting in the enlargement of one-dimensional pores, the formation of μ-bridging water molecules, and an increased spatial proximity between guest water and acidic bridging water. These structural changes facilitated efficient proton transport, resulting in an increase in conductivity from 7.23×10^{-5} to 2.50×10^{-3} S cm^{-1} at 363 K under 95% RH. Notably, while Y-DSNDC exhibited a conductivity drop at elevated temperature due to the release of weakly bound water molecules, K-DSNDC maintained higher conductivity compared to previously reported K-based coordination polymers, reflecting the thermal stability of its proton-conducting pathways. This study demonstrates that metal exchange provides an effective approach to tailor coordination environments and enhance proton conduction in CPs.

Author contributions

B. G. L., J. Y. B. and J. W. J. conducted the synthesis, characterization, and data analysis. D. K. performed the crystallographic analysis. D.-W. L. planned the research. All authors contributed to discussions and manuscript writing.

Conflicts of interest

There are no conflicts to declare.

Data availability

Supplementary information: Crystal structures, optical images, PXRD, FT-IR, XPS, TGA, vapor sorption, nyquist plots, crystallographic data, and proton conductivity table. See DOI: https://doi.org/10.1039/D5CE00639B.

CCDC 2463061 and 2463062 contains the supplementary crystallographic data for this paper.[49]

The authors confirm that the data supporting this article have been included as part of the SI. Crystallographic data for Y-DSNDC (CCDC2463061) and K-DSNDC (CCDC2463062) have been deposited at the Cambridge Crystallographic Data Center (CCDC).

Acknowledgements

Notes and references

1 K. Jiao, J. Xuan, Q. Du, Z. Bao, B. Xie, B. Wang, Y. Zhao, L. Fan, H. Wang, Z. Hou, S. Huo, N. P. Brandon, Y. Yin and M. D. Guiver, *Nature*, 2021, **595**, 361–369.

2 A. Kraytsberg and Y. Ein-Eli, *Energy Fuels*, 2014, **28**, 7303–7330.

3 R. Devanathan, *Energy Environ. Sci.*, 2008, **1**, 101–119.

4 D. E. Curtin, R. D. Lousenberg, T. J. Henry, P. C. Tangeman and M. E. Tisack, *J. Power Sources*, 2004, **131**, 41–48.

5 S. J. Lee, S. Mukerjee, J. McBreen, Y. W. Rho, Y. T. Kho and T. H. Lee, *Electrochim. Acta*, 1998, **43**, 3693–3701.

6 Y.-R. Liu, Y.-Y. Chen, Q. Zhuang and G. Li, *Coord. Chem. Rev.*, 2022, **471**, 214740.

7 M. A. Hickner, H. Ghassemi, Y. S. Kim, B. R. Einsla and J. E. McGrath, *Chem. Rev.*, 2004, **104**, 4587–4612.

8 D. Mukherjee, A. Saha, S. Moni, D. Volkmer and M. C. Das, *J. Am. Chem. Soc.*, 2025, **147**, 5515–5553.

9 T. Yamada, K. Otsubo, R. Makiura and H. Kitagawa, *Chem. Soc. Rev.*, 2013, **42**, 6655–6669.

10 S. M. Elahi, S. Chand, W.-H. Deng, A. Pal and M. C. Das, *Angew. Chem., Int. Ed.*, 2018, **57**, 6662–6666.

11 M. K. Sarango-Ramírez, D.-W. Lim, D. I. Kolokolov, A. E. Khudozhitkov, A. G. Stepanov and H. Kitagawa, *J. Am. Chem. Soc.*, 2020, **142**, 6861–6865.

12 R. Sahoo, S. C. Pal and M. C. Das, *ACS Energy Lett.*, 2022, **7**, 4490–4500.

13 S. C. Pal, S. Chand, A. G. Kumar, P. G. M. Mileo, I. Silverwood, G. Maurin, S. Banerjee, S. M. Elahi and M. C. Das, *J. Mater. Chem. A*, 2020, **8**, 7847–7853.

14 S. C. Pal, D. Mukherjee, Y. Oruganti, B. G. Lee, D.-W. Lim, B. Pramanik, A. K. Manna and M. C. Das, *J. Am. Chem. Soc.*, 2024, **146**, 14546–14557.

15 D. Mukherjee, S. C. Pal, Y. Oruganti, B. G. Lee, A. K. Manna, D.-W. Lim and M. C. Das, *ACS Energy Lett.*, 2025, **10**, 1216–1228.

16 Y. Oruganti, D. Kim and D.-W. Lim, *Cryst. Growth Des.*, 2024, **24**, 1612–1618.

17 P.-H. Wang, Y. Yoshida, S. Yasaka, M. Maesato, Y. Nakano and H. Kitagawa, *J. Am. Chem. Soc.*, 2025, **147**, 3804–3812.

18 F. Yang, G. Xu, Y. Dou, B. Wang, H. Zhang, H. Wu, W. Zhou, J.-R. Li and B. Chen, *Nat. Energy*, 2017, **2**, 877–883.

19 H. K. Lee, Y. Oruganti, J. Lee, S. Han, J. Kim, D. Moon, M. Kim, D.-W. Lim and H. R. Moon, *J. Mater. Chem. A*, 2024, **12**, 795–801.

20 N. C. Jeong, B. Samanta, C. Y. Lee, O. K. Farha and J. T. Hupp, *J. Am. Chem. Soc.*, 2012, **134**, 51–54.

21 P. Rought, C. Marsh, S. Pili, I. P. Silverwood, V. G. Sakai, M. Li, M. S. Brown, S. P. Argent, I. Vitorica-Yrezabal, G. Whitehead, M. R. Warren, S. Yang and M. Schröder, *Chem. Sci.*, 2019, **10**, 1492–1499.

22 W. J. Phang, H. Jo, W. R. Lee, J. H. Song, K. Yoo, B. Kim and C. S. Hong, *Angew. Chem., Int. Ed.*, 2015, **54**, 5142–5146.

23 D.-W. Lim, M. Sadakiyo and H. Kitagawa, *Chem. Sci.*, 2019, **10**, 16–33.

24 R. Liu, L. Zhao, S. Yu, X. Liang, Z. Li and G. Li, *Inorg. Chem.*, 2018, **57**, 11560–11568.

25 Q.-M. Wang, F.-Q. Jiang, R. Zhang, X.-X. Huang, J. Zheng, W.-W. Dong, D. Ba, J. Zhao and D.-S. Li, *J. Solid State Chem.*, 2024, **335**, 124696.

26 F.-M. Zhang, L.-Z. Dong, J.-S. Qin, W. Guan, J. Liu, S.-L. Li, M. Lu, Y.-Q. Lan, Z.-M. Su and H.-C. Zhou, *J. Am. Chem. Soc.*, 2017, **139**, 6183–6189.

27 V. G. Ponomareva, K. A. Kovalenko, A. P. Chupakhin, D. N. Dybtsev, E. S. Shutova and V. P. Fedin, *J. Am. Chem. Soc.*, 2012, **134**, 15640–15643.

28 D.-W. Lim and H. Kitagawa, *Chem. Rev.*, 2020, **120**, 8416–8467.

29 D.-W. Lim and H. Kitagawa, *Chem. Soc. Rev.*, 2021, **50**, 6349–6368.

30 S. Mukhopadhyay, J. Debgupta, C. Singh, R. Sarkar, O. Basu and S. K. Das, *ACS Appl. Mater. Interfaces*, 2019, **11**, 13423–13432.

31 S. Wang, M. Wahiduzzaman, L. Davis, A. Tissot, W. Shepard, J. Marrot, C. Martineau-Corcos, D. Hamdane, G. Maurin, S. Devautour-Vinot and C. Serre, *Nat. Commun.*, 2018, **9**, 4937.

32 M. Sadakiyo, T. Yamada and H. Kitagawa, *J. Am. Chem. Soc.*, 2014, **136**, 13166–13169.

33 K. Otake and H. Kitagawa, *Small*, 2021, **17**, 2006189.

34 C.-X. Yu, H. Wu, Z. Shao, M.-J. Gao, X.-Q. Sun and L.-L. Liu, *Inorg. Chem.*, 2025, **64**, 3908–3916.

35 A. Goswami, A. Ghorai, D. Pal, S. Banerjee and K. Biradha, *Chem. – Eur. J.*, 2024, **30**, e202402165.

36 H. Wang, Q. Wu, X. Ding, Z. Shao, W. Xu, Y. Zhao, Q. Xie, X. Meng and H. Hou, *Inorg. Chem.*, 2020, **59**, 8361–8368.

37 L.-L. Kang, M. Xue, Y.-Y. Liu, Y.-H. Yu, Y.-R. Liu and G. Li, *Coord. Chem. Rev.*, 2022, **452**, 214301.

38 W.-W. Wu, J.-J. Cai, X.-Y. Liang, Z.-Z. Li, S. Andra, K. Gao, H.-J. Lun and Y.-M. Li, *ACS Appl. Mater. Interfaces*, 2024, **16**, 68358–68367.

39 B. F. Abrahams, C. J. Commons, T. A. Hudson, R. S. Arlt, K. F. White, M. Chang, J. J. Jackowski, M. Lee, S. X. Lee, H. D. Liu, B. M. Mei, J. E. Meng, L. Poon, X. Xu and Z. Yu, *Acta Crystallogr., Sect. C: Struct. Chem.*, 2021, **77**, 340–353.

40 K. Saito, M. Nakagawa and H. Ishikita, *Commun. Chem.*, 2020, **3**, 89.

41 O. Bistri and O. Reinaud, *Org. Biomol. Chem.*, 2015, **13**, 2849–2865.

42 M. E. A. Safy, M. Amin, R. R. Haikal, B. Elshazly, J. Wang, Y. Wang, C. Wöll and M. H. Alkordi, *Chem. – Eur. J.*, 2020, **26**, 7109–7117.

43 S. Alvarez, P. Alemany, D. Casanova, J. Cirera, M. Llunell and D. Avnir, *Coord. Chem. Rev.*, 2005, **249**, 1693–1708.

44 Q.-Y. Liu, W.-F. Wang, Y.-L. Wang, Z.-M. Shan, M.-S. Wang and J. Tang, *Inorg. Chem.*, 2012, **51**, 2381–2392.

45 M. A. Al-Ghouti and D. A. Da'ana, *J. Hazard. Mater.*, 2020, **393**, 122383.

46 P. Zhang, *Adsorption and Desorption Isotherms*, 2016.

47 M. Bazaga-García, M. Papadaki, R. M. P. Colodrero, P. Olivera-Pastor, E. R. Losilla, B. Nieto-Ortega, M. Á. G. Aranda, D. Choquesillo-Lazarte, A. Cabeza and K. D. Demadis, *Chem. Mater.*, 2015, **27**, 424–435.

48 N. Sikdar, D. Dutta, R. Haldar, T. Ray, A. Hazra, A. J. Bhattacharyya and T. K. Maji, *J. Phys. Chem. C*, 2016, **120**, 13622–13629.

49 (*a*) B. G. Lee, D. Kim, J. Y. Bae, J. W. Jeong and D.-W. Lim, CCDC 2463061: Experimental Crystal Structure Determination, 2025, DOI: **10.5517/ccdc.csd.cc2np0lz**; (*b*) B. G. Lee, D. Kim, J. Y. Bae, J. W. Jeong and D.-W. Lim, CCDC 2463062: Experimental Crystal Structure Determination, 2025, DOI: **10.5517/ccdc.csd.cc2np0m0**.